LAWRENCE
LIVERMORE
NATIONAL
LABORATORY

An optimal point spread function subtraction algorithm for high-contrast imaging: a demonstration with angular differential imaging

D. Lafreniere, C. Marois, R. Doyon, E. Artigau, D. Nadeau

September 22, 2006

Disclaimer

An optimal point spread function subtraction algorithm for high-contrast imaging: a demonstration with angular differential imaging [1]

David Lafrenière[2], Christian Marois[2,3], René Doyon[2], Étienne Artigau[2] and Daniel Nadeau[2]

david@astro.umontreal.ca cmarois@igpp.ucllnl.org
doyon@astro.umontreal.ca artigau@astro.umontreal.ca
nadeau@astro.umontreal.ca

ABSTRACT

Direct imaging of exoplanets is limited by bright quasi-static speckles in the point spread function (PSF) of the central star. This limitation can be reduced by subtraction of reference PSF images. We have developed an algorithm to construct an optimal reference PSF image from an arbitrary set of reference images. This image is built as a linear combination of all available images and is optimized independently inside multiple subsections of the image to ensure that the *absolute* minimum residual noise is achieved within each subsection. The algorithm developed is completely general and can be used with many high-contrast imaging observing strategies, such as angular differential imaging (ADI), roll subtraction, spectral differential imaging, reference star observations, etc. The performance of the algorithm is demonstrated for ADI data. It is shown that for this type of data the new algorithm provides a gain in sensitivity by up to a factor 3 at small separation over the algorithm previously used.

Subject headings: Instrumentation: adaptive optics — planetary systems — stars: imaging — techniques: image processing — techniques: high angular resolution

Suggested running page header: PSF subtraction in high-contrast imaging

[2]Département de physique and Observatoire du Mont Mégantic, Université de Montréal, C.P. 6128, Succ. Centre-Ville, Montréal, QC, Canada H3C 3J7

[3]Institute of Geophysics and Planetary Physics L-413, Lawrence Livermore National Laboratory, 7000 East Ave, Livermore, CA 94550

1. Introduction

Direct imaging of exoplanets, circumstellar disks, jets, winds or other structures around stars is difficult due to the angular proximity of the star and the very large luminosity ratios involved. Current attempts, both from the ground with adaptive optics (AO) and from space, are limited by a swarm of bright quasi-static speckles that completely mask out the faint planets or structures that are sought after (Marois et al. 2003, 2005). These speckles, which are mainly caused by imperfections in the optics, are long-lived, hence the "quasi-static" appellation, and do not average out during a long observation. As a result, increasing further the integration time after a few minutes hardly provides any gain in detection sensitivity (Marois et al. 2005; Masciadri et al. 2005).

Several techniques have been developed to work around this limitation and the most successful with existing instruments subtract the speckles by using reference point spread function (PSF) images. This too is a difficult task because even though the speckles are long lived, they still vary with time due to temperature or pressure changes, mechanical flexures, guiding errors or other phenomena (Marois et al. 2005, 2006). On the other hand, even when a reference PSF is acquired simultaneously with the science image at other wavelengths or polarizations, differential aberrations within the camera decorrelate the PSFs (Marois et al. 2003, 2005; Lenzen et al. 2004). Thus, when trying to subtract speckles one must always work with slightly decorrelated reference PSF images and the specific way in which the available data are used to perform the subtraction may have a significant impact on the speckle noise attenuation achieved. This paper presents an optimal way of using a set of reference PSF images to achieve the best attenuation possible. In particular the technique is applied to angular differential imaging (ADI) (Marois et al. 2006), which is currently one of the most efficient speckle suppression technique for ground-based observations. Although emphasis is given to exoplanet detection throughout the paper, the reader should keep in mind that the algorithm can be used to search for any other structure in the close vicinity of a star.

The new reference PSF construction algorithm is presented in Sect. 2. Then, a review of ADI and of the algorithm used by Marois et al. (2006) is presented in Sect. 3. In Sect. 4, the new algorithm is applied to ADI and its performance is presented. The possibility of using this algorithm with other observing strategies is finally discussed in Sect. 5.

2. New reference PSF image construction algorithm

Given an arbitrary set of PSF images including observations of a target, we propose to construct, for each image of the target, a reference PSF image as a linear combination of all

"suitable" reference images available. A reference image is considered suitable if its subtraction would not remove a companion point source. The simplest example of suitable reference images would be observations of one or more reference stars, but there are many other, more elaborate, possibilities such as ADI, roll subtraction, spectral differential imaging, etc. These will be briefly discussed in Sect. 5. The coefficients of the linear combination are obtained by minimization of the noise in the residual image after subtraction. By using *all* the PSF information available and allowing each image to weigh differently in the combination, this approach generally produces a better representation of the PSF under consideration. We now derive the general formalism for the construction of a reference PSF image from a set $\{I^n : n = 1, 2 \ldots N\}$ of images of the target and possibly reference stars.

Generally, the evolution of the PSF speckle pattern through the sequence $\{I^n\}$ varies with spatial position. For example, a slow drift of the PSF over the detector would lead to a more rapid evolution of the speckle pattern along the direction of the drift (Marois et al. 2005). Hence, an image of the sequence may show a poor correlation with another image in a region aligned with the drift but a high correlation in a region in the perpendicular direction. It is thus desirable to independently construct a reference PSF image over subsections of the image rather than over the whole image at once. This allows a better representation of local differential evolution of the PSF speckle pattern. This is the method we use and the algorithm described below applies to one such region. Particularly, it is implicit in the remainder of the section that I^n refers to a region of image n. Note that one could always, if desired, use a single region consisting of the whole image. Also, one needs not subtract the optimized reference over the entire region over which it was optimized. An extreme example of this is to use a different optimization region for each pixel and apply the subtraction of the optimized reference to the given pixel only; however, this procedure is computationally prohibitive. An intermediate possibility is to subtract the optimized reference PSF image over a subsection of the optimization region, and then define another optimization region for subtraction of a different set of pixels. An example of this procedure will be given later. The best approach to use depends on the specific data being analyzed and the algorithm described below is not restricted to a particular one.

From the point of view of the algorithm, a companion point source is a residual and thus it will be partially subtracted. The importance of this effect, or the amount of partial subtraction, depends upon the fraction of the region area that is occupied by the point source. So, even though smaller regions lead to a better fit of the PSF structure, hence to a better noise attenuation, they also lead to a larger subtraction of the signal of the point sources sought after. Thus the size of the regions over which the algorithm is applied must be properly optimized and the amount of partial subtraction of point sources must be well characterized. The area A of the regions is determined by the parameter N_A through the

96   expression

$$A = N_A \, \pi \left(\frac{W}{2} \right)^2 \tag{1}$$

where W is the FWHM of the PSF; N_A thus corresponds to the number of "PSF cores" that
98   fit in a region.

The subset of images used to construct a reference PSF generally varies with the image,
100   I^n, from which the speckles are to be subtracted. It includes all images in which a companion
point source would be displaced by at least a distance $\delta_{\min}$ or would have an intensity smaller
102   by at least a factor α with respect to its position or intensity in I^n. This set is formally
defined as $\{ I^k : k \in K^n \}$, where

$$K^n = \{ k \in [1, N] \; : \; |\mathbf{r}_k - \mathbf{r}_n| > \delta_{\min} \; \vee \; f_k / f_n < \alpha \} \tag{2}$$

104   and $\mathbf{r}_n$ and f_n respectively denote the position and intensity relative to the central star of
any companion or background source in the given region of image n.

106   The reference PSF R^n is then constructed according to

$$R^n = \sum_{k \in K^n} c^k I^k \tag{3}$$

where the coefficients c^k are to be determined by the algorithm. They are computed by
108   minimizing the sum of the square of the residuals after subtraction of the reference region,
which is given by

$$\sigma^2 = \sum_i m_i \, (I_i^n - R_i^n)^2 = \sum_i m_i \left(I_i^n - \sum_k c^k I_i^k \right)^2 \tag{4}$$

110   where i denotes a pixel in the region considered and m is a binary mask that may be used
to ignore some pixels. The quantity to minimize is a sum and can be biased by cosmic ray
112   hits or bad pixels if they have not been properly corrected or filtered before the algorithm is
used. When bad pixels remain in the image, the bias can be completely remedied by setting
114   the mask m to zero for these pixels. Generally, the fraction of pixels affected is very small
and their exclusion from the computation of the residuals has practically no impact on the
116   solution found. The minimum of σ^2 occurs when all its partial derivatives with respect to
the coefficients c^k are equal to zero, i.e. when

$$\frac{\partial \sigma^2}{\partial c^j} = \sum_i -2m_i I_i^j \left(I_i^n - \sum_k c^k I_i^k \right) = 0 \quad \forall \, j \in K^n \tag{5}$$

Reversing the summation order and rearranging the terms we find

$$\sum_k c^k \left(\sum_i m_i I_i^j I_i^k \right) = \sum_i m_i I_i^j I_i^n \quad \forall \, j \in K^n \tag{6}$$

This is a simple system of linear equations of the form $\mathbf{Ax} = \mathbf{b}$ where

$$A_{jk} = \sum_i m_i I_i^j I_i^k \quad \text{and} \tag{7}$$

$$b_j = \sum_i m_i I_i^j I_i^n \tag{8}$$

Solving this system gives the coefficients c^k needed to construct the reference region and perform the subtraction. By construction, assuming that all the I^k are linearly independent, the matrix $\mathbf{A}$ is always invertible. Thus, the system always has a unique solution, meaning that for a given region and set K^n the solution found is an *absolute* minimum of the residuals.

3.   Review of ADI

The ADI technique, detailed in Marois et al. (2006), consists in acquiring a sequence of many exposures of the target using an altitude/azimuth telescope with the instrument rotator turned off (at the Cassegrain focus) or adjusted (at the Nasmyth focus) to keep the instrument and telescope optics aligned. This is the most stable configuration and ensures the highest correlation of the sequence of PSF images. This setup also causes a rotation of the field of view (FOV) during the sequence. For each image, a reference image is built from a combination of other images of the same set. Because of the FOV rotation, a companion would appear at different angular positions with respect to the PSF in different exposures and hence would not be removed by the subtraction if images with sufficient FOV rotation are used to build the reference. After speckle subtraction, the residual images are rotated to align the FOV and co-added. Because of the rotation, the PSF residual speckle noise is averaged incoherently, ensuring an ever improving detection limit with increasing exposure time.

As shown in Fig. 2 of Marois et al. (2006), the correlation between two images of a sequence decreases as a function of the time delay between them; hence, one would want to use images obtained as close in time as possible to build the reference image as this would lead to a better speckle noise attenuation. However, one has to make sure that the FOV rotation between an image and the ones used to build the reference is sufficient to displace a point source by at least $\delta_{\min}$. The time delay $\tau_{\min}$ required for such a FOV rotation decreases as the inverse of the angular separation. Accordingly, it is possible to use more closely separated images to subtract speckles at larger angular separations. Eq. 1 and Fig. 1 of Marois et al. (2006) may be used to calculate $\tau_{\min}$.

We recall here the speckle subtraction algorithm used by Marois et al. (2006) (see their Sect. 5.2 and their Table 2) since it will be used later for comparison with the new algorithm. Their first step, after basic data reduction, is to subtract the median of all the images from each individual image (in the context of the new algorithm, this is similar to setting $c_k = 1/N \; \forall \; k$). Given that enough FOV rotation has occurred during the sequence, a point source would be largely rejected by the median and would survive this subtraction. Then an optimized reference image is obtained for each image by median combining four images (two acquired before and two after) having a FOV orientation difference providing a point source displacement of at least 1.5 PSF FWHM. During the process, the image is broken into many annuli of width equal to 7 PSF FWHM to accommodate the dependence of $\tau_{\min}$ on the separation. The intensity of the reference PSF is then scaled appropriately inside each annulus to minimize the noise after subtraction. The intensity scaling factor converges to zero if the annulus is dominated by pixel-to-pixel noise or to unity if it is dominated by correlated speckles. The optimized reference PSF is then subtracted. All the resulting images are then rotated to align the FOV to that of the first image and a median is taken over them.

4. ADI with the new algorithm

4.1. Definition of the regions and determination of $\delta_{\min}$

The application to ADI of the algorithm described in Sect. 2 is straightforward. First, we need to define the geometry of the regions. The dependence of $\tau_{\min}$ on angular separation suggests the use of annular regions. The annuli are further divided into sections to enable a better fit of local PSF variations. Since $\tau_{\min}$ is proportional to $1/r$, the set of images that can be used to construct a reference PSF changes rapidly with radius at small separation and it is best to use narrow annuli to ensure that the largest set of reference images is used at all separations. However, maintaining a given area using narrow annuli requires

sections of large azimuthal extent which are not optimal to adapt to local variations of the PSF speckle pattern. Therefore, we optimize the reference PSF using a wider, hence more compact, section of annulus but we subtract the optimized reference over only the inner pixels (smaller radius) of this region. We extend the optimization region outward of the subtraction region because the radial dependence of the PSF noise naturally gives more weight in the optimization to the inner pixels. The same process is repeated until the subtraction has been applied to all pixels. This procedure yields the optimal set of reference images and region shape for all separations. Fig. 1 shows an example of regions that can be used with this procedure.

The optimization regions are defined by their inner radius r, mean angular position ϕ, radial width Δr and angular width $\Delta\phi$ and can be characterized by only two parameters: N_A and g, where $g = \Delta r^2/A$. The parameter g defines the overall shape of the regions: their radial width is roughly g times their azimuthal width. The subtraction of the optimized reference is done only over the inner width dr of the optimization region; dr is expressed in units of the PSF FWHM.

Then, for the optimization region $(r, \Delta r, \phi, \Delta\phi)$ of image I^n, the minimum displacement $\delta_{\min}$ is defined by the expression

$$\delta_{\min} = N_\delta W + r\,d\theta_n \qquad (9)$$

where N_δ represents the minimum gap allowed, in units of the PSF FWHM, between a source position in image n and the corresponding positions in the images used a references, and $d\theta_n$ is the angle of FOV rotation that occurred during exposure n. The last term of the expression above represents the azimuthal smearing of an off-axis point source that occurs during an exposure due to FOV rotation.

The values of N_A, g, dr and N_δ that maximize the sensitivity to faint point sources will be determined in the next section using real data.

4.2.   Parameter optimization

Observations of the star HD97334b (G0V, $H = 5$) were used to optimize the values of the algorithm parameters. These observations are part of the Gemini Deep Planet Survey (GDPS, D. Lafrenière et al., in preparation), which is an ongoing direct imaging search for Jupiter mass planets on large orbits (> 40 pc) around young nearby stars ($\sim$100 Myr). This particular dataset consists in a sequence of 90 30-s images in the CH$_4$-short (1.58 μm, 6.5%)

filter obtained with ALTAIR/NIRI at the Gemini North telescope (program GN-2005A-Q-16). These images are saturated inside a radius of $\sim 0\rlap{.}''7$ from the PSF center. Short unsaturated exposures were acquired before and after the saturated sequence to calibrate photometry and detection limits. The corrected PSF FWHM was measured to be 74 milliarcseconds, or 3.4 pixels, and the Strehl ratio was $\sim 14\%$. The Cassegrain rotator was fixed during all observations. Basic image reduction and registering was done as in Marois et al. (2006).

The same procedure was used for optimizing each of N_δ, N_A, g and dr. First, the unsaturated PSF image, properly smeared azimuthally for each image and angular separation, was used to produce artificial point sources that were added to the reduced images at angular separations in the range 50-300 pixels (27-160 λ/D) in steps of 5 pixels (2.75 λ/D). The intensities of the artificial sources were set so that their S/N would be ~ 10 in the final residual combination. Next, a symmetric radial profile was subtracted from each image to remove the seeing halo. Then the subtraction algorithm was executed on the sequence of images with a range of values for the parameter under consideration. Finally, the noise and the flux of each artificial point source in an aperture diameter of one FWHM were measured in the residual image. This process was repeated 50 times by placing the artificial sources at different angular positions each time. The trial values for the optimization of each parameter are listed in Table 1. When optimizing a given parameter, all other parameters were set to their optimal value except for dr which was set to 1.5. The results are shown in Fig. 2-5.

As it can be seen in Fig. 2, the minimum spacing has little impact on the recovered flux at large separations, where ~ 80-90% of the flux is recovered independently of N_δ. However, at small separations the effect is important and significant loss in signal occurs, particularly for the smallest minimum displacements. This is because the fraction of images in the set K^n for which the point source partially overlaps that in image n is greater for small separations, where linear motion of the point source is slower. Nevertheless, the best overall S/N is obtained with $N_\delta = 0.5$, which corresponds to a relatively small minimum displacement.

Figure 3 shows that the residual signal of the point sources is strongly dependent upon the size of the regions, as expected from the discussion of Sect. 2. Regions with N_A too small do not yield a sufficient gain in attenuation to compensate for the larger point source subtraction and yield lower S/N ratios, especially at large separations. On the other hand, regions with N_A too large do not subtract speckles as efficiently at small separations and yield lower S/N ratios. A value of $N_A = 300$ provides the best overall S/N ratio.

The parameter g has little effect on the performance, see Fig. 4. Although it appears that regions more extended azimuthally ($g = 0.5$) fare slighlty worse at small separations and regions more extended radially fare slightly better over a very small interval. Nevertheless,

we adopt $g = 1$ as the optimal value.

Finally, Fig. 5 shows that at small separations, large values of dr lead to lower S/N ratios because they poorly match the evolution of τ_{min} with separation, as expected. At large separations, larger values of dr do very slightly better. Since a larger dr leads to a faster execution of the algorithm, because a larger fraction of the optimization region is actually subtracted, a trial was made with dr equal to 1.5 at small separations and 15 at large separations with a smooth transition at a separation of 60 λ/D. This is what we use as the optimal value.

The optimal parameter values may vary slightly from those found above for another set of data depending on the telescope, instrument, seeing, FOV rotation rate, target brightness, etc. They are optimized here for a specific set of data only to illustrate the full potential of the new algorithm for ADI. For all computations that follow, the optimal values listed in Table 1 are always used.

4.3. Point source photometry

Since the algorithm reduces the flux of point sources significantly, especially at small separations, it is important to verify that the true flux can be recovered accurately and that the uncertainty on this value can be well determined. We have run the algorithm on the sequence of images with artificial companions of various intensities at all angular separations in the range 50-300 pixels (27-160 λ/D) by steps of 5 pixels (2.75 λ/D). Four intensities were used, yielding S/N of 3, 6, 10 and 25 in the final residual image. This process was repeated 50 times with the sources at different angular positions. The mean normalized residual source intensities and residual intensity dispersions over the 50 angular positions were then computed; Fig. 6 shows the results.

The top panel of this figure shows that the normalized residual intensities do not vary with the intensity of the sources, i.e. *the fraction of the flux subtracted by the algorithm is independent of the source brightness.* Hence, a normalized residual intensity curve obtained by implanting artificial point sources of a given brightness can be used to recover the true flux of sources of any brightness. In particular, it may be used to correct the detection limit curve computed from the variance of the residual noise. The bottom panel of Fig. 6 shows that the noise measured in the residual image is an adequate measure of the dispersion of the source intensities for sources at 10σ or less. For brighter sources ($\sim25\sigma$), the dispersion in residual intensity increases slightly for small separations. This is probably due to the larger bias introduced by brighter point sources and the more important dependence of the amount

of partial subtraction on the specific PSF structure underlying the point source in regions strongly dominated by speckle noise. Thus, the noise in the residuals may be used as the uncertainty on the flux for most sources but it may be necessary to carry out an analysis using artificial point sources for brighter sources at small separations.

4.4. Comparison with previous algorithm

A comparison of the new algorithm with that used by Marois et al. (2006) is presented. Artificial point sources were added to the images at several separations in the range 40-500 pixels (22-275 λ/D) by steps of 5 pixels (2.75 λ/D). The intensities of the artificial sources were adjusted to yield a final S/N∼10 with the new algorithm. Both subtraction algorithms were then run on the images. This was repeated 25 times with the artificial sources at different angular positions. The mean residual intensity and S/N over the 25 angular positions were then computed for each algorithm and separation. The results are shown in Fig. 7. The new algorithm yields a better S/N at all separations. The gain is highest at small separations, where it reaches a factor ∼3, and steadily decreases for larger separations. The decrease is most likely due to the increasing relative importance of sky background noise. A comparison of the residual image of the two algorithms is shown in Fig. 8; the lower level of noise of the new algorithm is clearly visible. The new algorithm yields a better attenuation because it can adapt more easily to temporal and spatial variations of the PSF speckle pattern by using all the images available with proper weights (the coefficients) and optimizing the reference in smaller regions.

The subtraction algorithms were then applied to the original sequence of images, i.e. without artificial sources, to compare the speckle noise attenuation they provide and the detection limits they achieve. The speckle noise attenuation is shown in Fig. 9; a single subtraction using the new algorithm provides an attenuation of ∼10-12 at separations of 1-3 arcsec. The formulation of a simple and universal criterion for speckle-limited point source detection is usually complicated because the distribution of speckle noise is non Gaussian (Schneider & Silverstone 2003; Aime & Soummer 2004; Marois 2004; Fitzgerald & Graham 2006); it possesses an important tail at the higher end. However, ADI leads to residuals whose distribution closely resembles a Gaussian; this is studied in more detail elsewhere (C. Marois et al., in preparation). This was indeed verified for the data presented here, see Fig. 10; a few events above a Gaussian distribution are seen only at the smallest angular separations. This figure indicates that a 5σ threshold is adequate for estimating detection limits. The final 5σ detection limits in difference of magnitudes reach 13.9, 16.1 and 16.9 at angular separations of 1, 2 and 3 arcsec respectively, see Fig. 11. The speckle noise

attenuation and the detection limits have been properly corrected for the partial loss of signal of point sources as measured from the residual signal of artificial sources.

Comparison of the two algorithms were made using a few different observation sequences and similar results were obtained every time.

5. Conclusion

An algorithm to construct a reference PSF image used to subtract the speckle noise and improve the sensitivity to faint companion detection was developed and tested. The algorithm combines many observations of the target or other stars to form, for each image of the target, a reference PSF image that minimizes the residuals after its subtraction. The reference PSF image produced by this algorithm yields the *absolute* minimum residual noise within the optimization regions used for a given set of reference images. The application of the algorithm to ADI yielded a factor of up to 3 improvement at small separations over the algorithm previously used.

The algorithm presented in Sect. 2 is general and can be used with most high contrast imaging observations aimed at finding point sources. In particular, it can be used with a sequence of images of the same target obtained at different FOV orientations (ADI, roll subtraction for HST (Schneider & Silverstone 2003), ground-based observations with discrete instrument rotations, etc.), with images of the same target at different wavelengths (simultaneous spectral differential imaging (SSDI) (Racine et al. 1999; Marois et al. 2000) or non-simultaneous spectral differential imaging (NSDI) with, for example, a tunable filter) or with images of similar targets acquired with the same instrument in a similar configuration. The latter could be particularly interesting for HST for which the PSF is more stable than at any ground-based telescope and for which suitable observations of reference stars may be readily retrieved from the archive. This should also be the case for the James Webb Space Telescope (JWST), whose temperature is expected to be much more stable as a result of its more stable environment. Future ground-based instrumentation designed specifically for finding exoplanets will have a small FOV, rendering SSDI inefficient to detect planets whose spectrum has no steep feature and ADI inefficient because of the very long time baseline required for sufficient rotation. For such cases, discrete instrument rotations may be critical and the algorithm developed here could be used directly. The Fine Guidance Sensor onboard JWST (Rowlands et al. 2004a), which will include a tunable filter imager (Rowlands et al. 2004b) and coronagraph (Doyon et al. 2004), is a very interesting prospect for NSDI. Again, the algorithm developed here could be directly applied to this case.

REFERENCES

Aime, C., & Soummer, R. 2004, ApJ, 612, L85

Doyon, R., Lafrenière, D., Rowlands, N., Evans, C., Murowinski, R., Hutchings, J. B., & Alexander, R. 2004, in Proc. SPIE, Vol. 5487, Optical, Infrared, and Millimeter Space Telescopes, ed. J. C. Mather, 746-753

Fitzgerald, M. P., & Graham, J. R. 2006, ApJ, 637, 541

Lenzen, R., Close, L., Brandner, W., Biller, B., & Hartung, M. 2004, in Proc. SPIE, Vol. 5492, Ground-based Instrumentation for Astronomy, ed. A. F. M. Moorwood & M. Iye, 970-977

Marois, C. 2004, Ph.D. Thesis

Marois, C., Doyon, R., Nadeau, D., Racine, R., Riopel, M., Vallée, P., & Lafrenière, D. 2005, PASP, 117, 745

Marois, C., Doyon, R., Nadeau, D., Racine, R., & Walker, G. A. H. 2003, in EAS Publications Series, Vol. 8, Astronomy with High Contrast Imaging, ed. C. Aime & R. Soummer, 233-243

Marois, C., Doyon, R., Racine, R., & Nadeau, D. 2000, PASP, 112, 91

Marois, C., Lafrenière, D., Doyon, R., Macintosh, B., & Nadeau, D. 2006, ApJ, 641, 556

Masciadri, E., Mundt, R., Henning, T., Alvarez, C., & Barrado y Navascués, D. 2005, ApJ, 625, 1004

Racine, R., Walker, G. A. H., Nadeau, D., Doyon, R., & Marois, C. 1999, PASP, 111, 587

366 Rowlands, N. 2004a, in Proc. SPIE, Vol. 5487, Optical, Infrared, and Millimeter Space
Telescopes, ed. J. C. Mather, 664-675

368 Rowlands, N. 2004b, in Proc. SPIE, Vol. 5487, Optical, Infrared, and Millimeter Space
Telescopes, ed. J. C. Mather, 676-687

370 Schneider, G., & Silverstone, M. D. 2003, in Proc. SPIE, Vol. 4860, High-Contrast Imaging
for Exo-Planet Detection, ed. A. B. Schultz, 1-9

Table 1: Parameter values used for optimization

Parameter	Trial values	Adopted value
N_δ	0.25, 0.5, 0.75, 1.0, 1.5, 2.0	0.5
N_A	50, 100, 150, 300, 500	300
g	0.5, 1.0, 2.0	1.0
dr	1.5, 3, 6, 9, 15, (1.5-15)[a]	(1.5-15)[a]

[a]dr equal to 1.5 at small separations and 15 at large separations with a smooth transition at a separation of 60 λ/D.
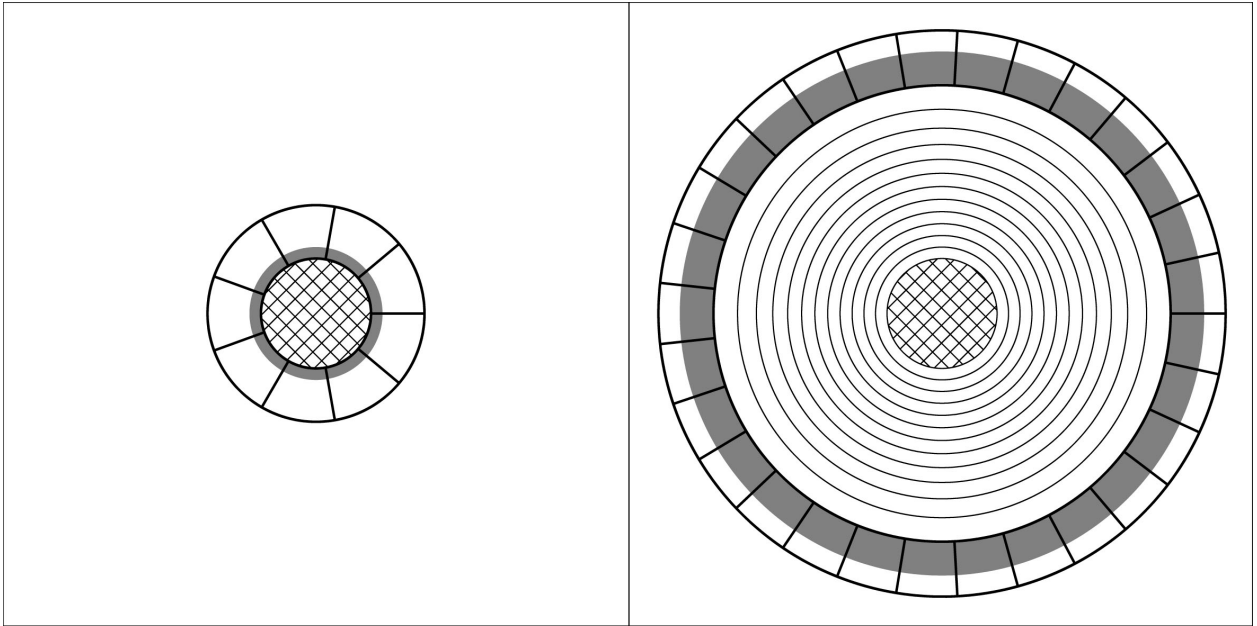
Fig. 1.— Example layout of regions for ADI using the procedure of Sect. 4.1. The subtraction of the optimized reference PSF is done inside the grey section of the optimization regions, which are represented by thick lines. The left and right panels show the optimization and subtraction regions for the 1st and 13th subtraction annuli respectively. In the right panel, the first 12 subtraction annuli, of width dr, are marked by thin lines; in this specific example, dr increases with radius. The central circle (cross-hatched) represents the saturated region.
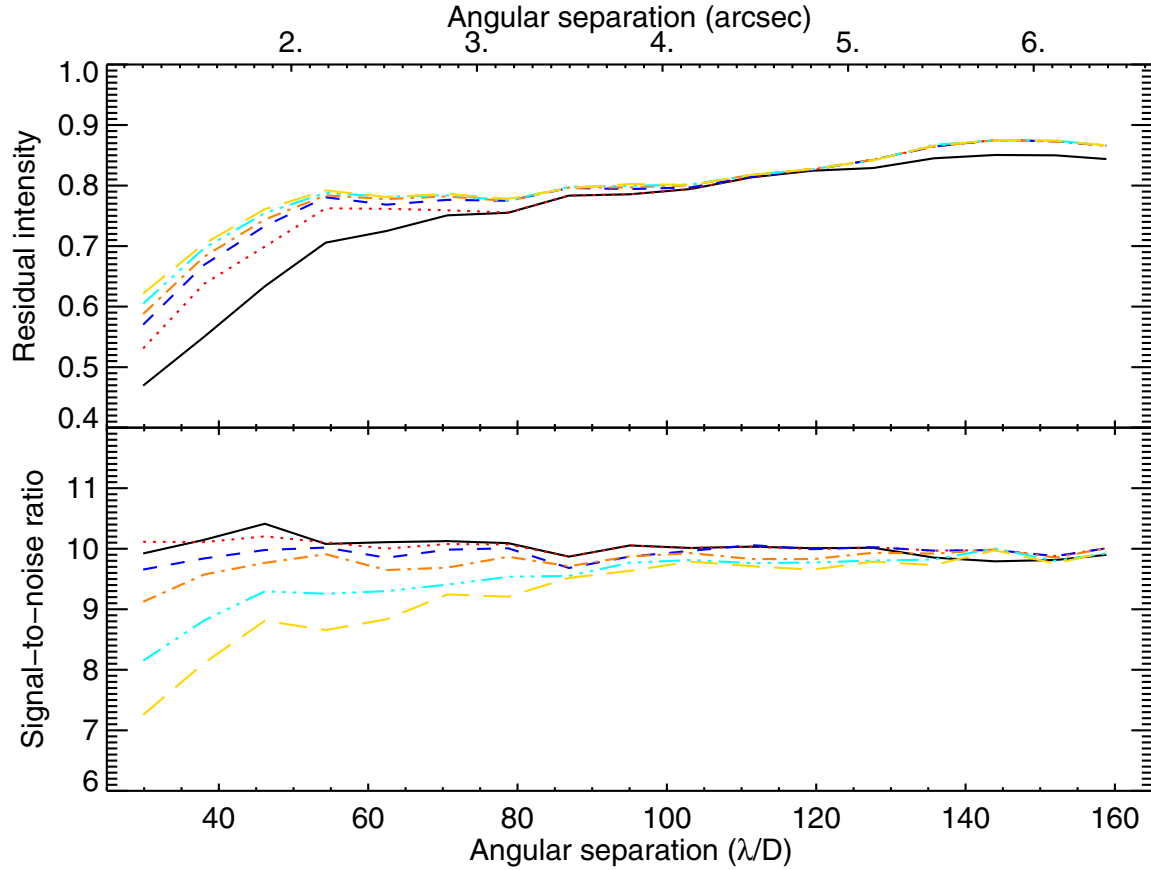
Fig. 2.— Average residual intensity of the artificial point sources normalized to their initial intensity (*top*) and their S/N ratio (*bottom*) as a function of angular separation. The solid (black in electronic edition), dotted (red), dashed (blue), dot-dashed (orange), triple-dot-dashed (aqua) and long-dashed (yellow) curves are respectively for $N_\delta = 0.25$, 0.5, 0.75, 1.0, 1.5 and 2.0.
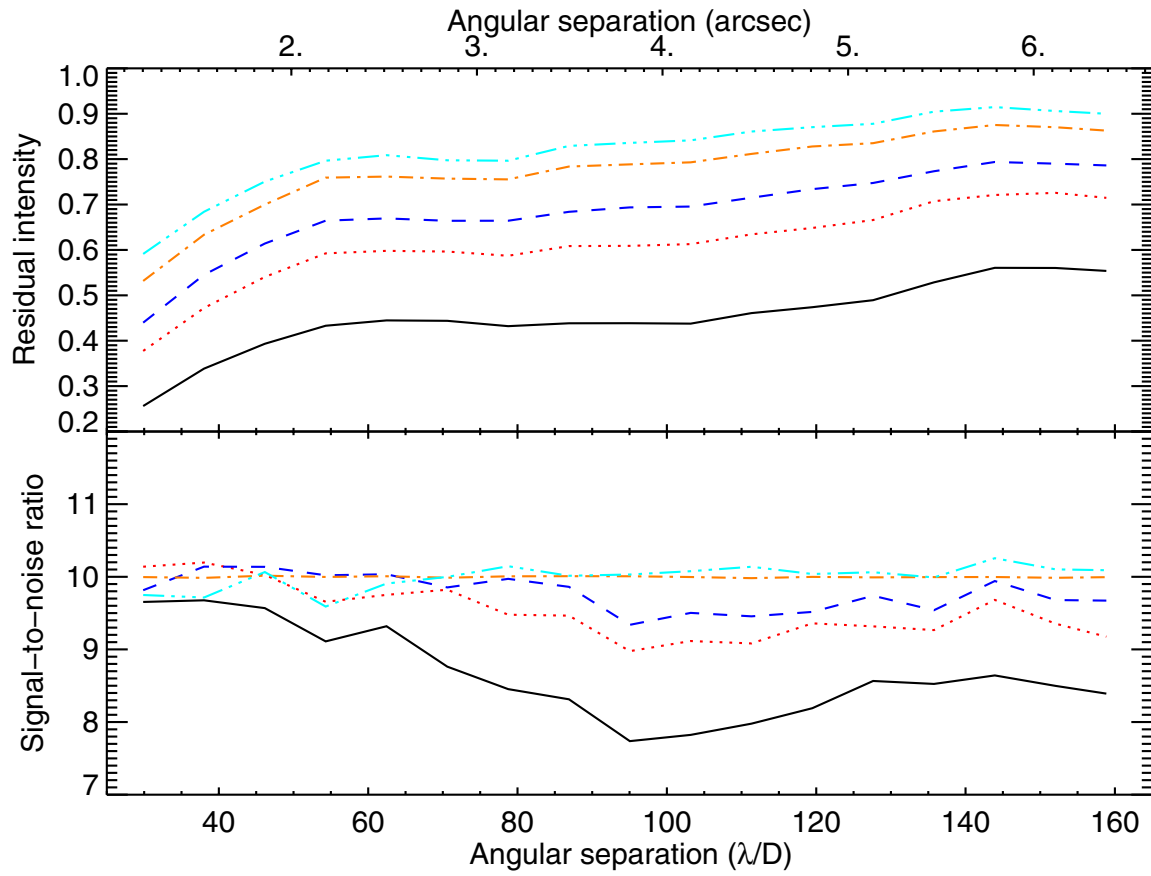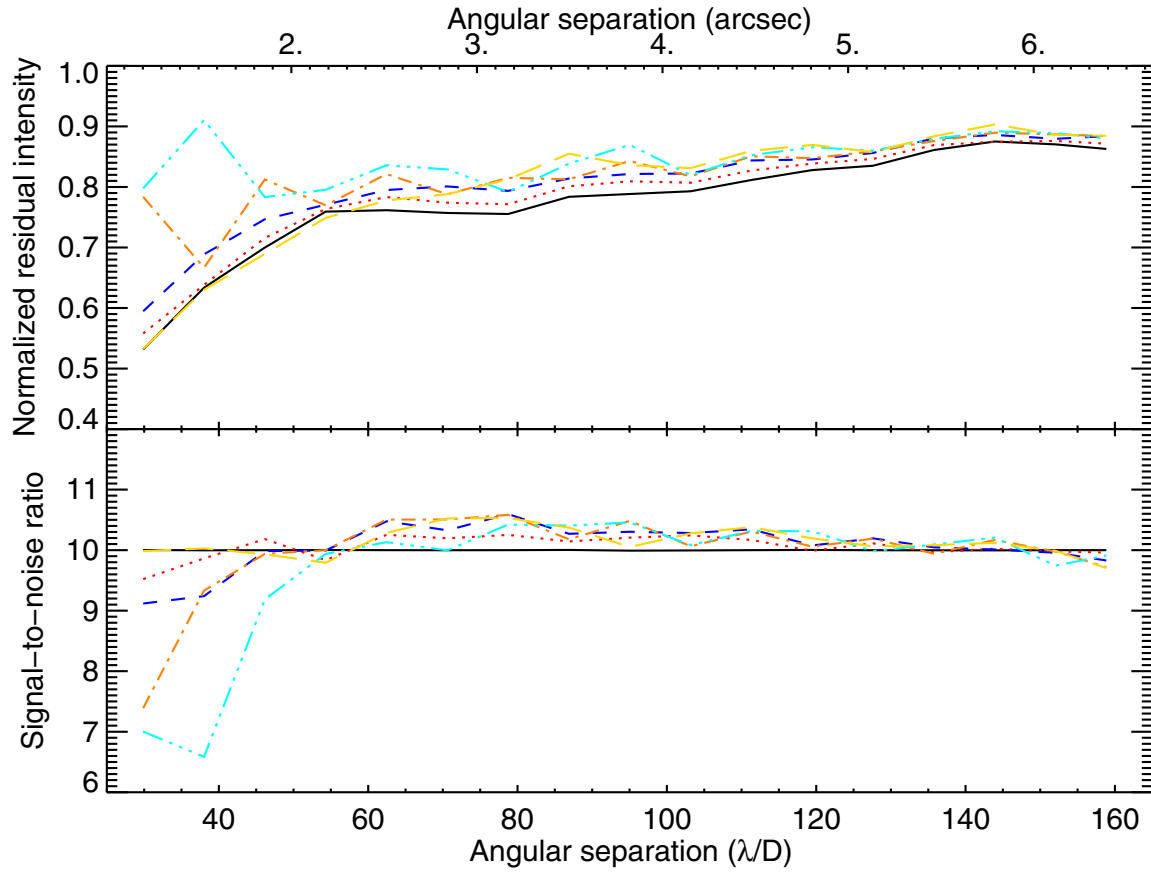
Fig. 3.— Same as Fig. 2. The solid (black), dotted (red), dashed (blue), dot-dashed (orange) and triple-dot-dashed (aqua) curves are respectively for $N_A = 50, 100, 150, 300$ and 500.
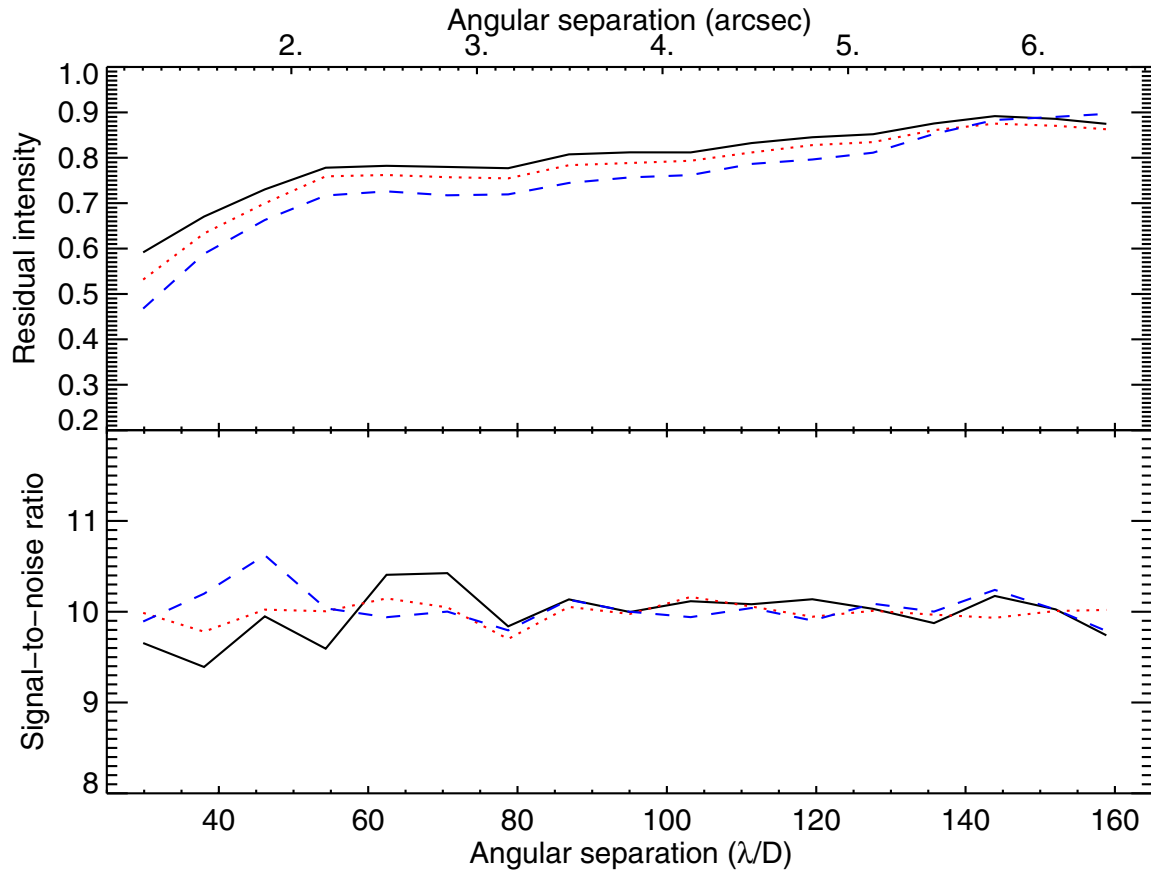
Fig. 4.— Same as Fig. 2. The solid (black), dotted (red) and dashed (blue) curves are respectively for $g = 0.5$, 1 and 2.

Fig. 5.— Same as Fig. 2. The solid (black), dotted (red), dashed (blue), dot-dashed (orange), triple-dot-dashed (aqua) and long-dashed (yellow) curves are respectively for dr = 1.5, 3, 6, 9, 15 and dr varying with radius (see text).
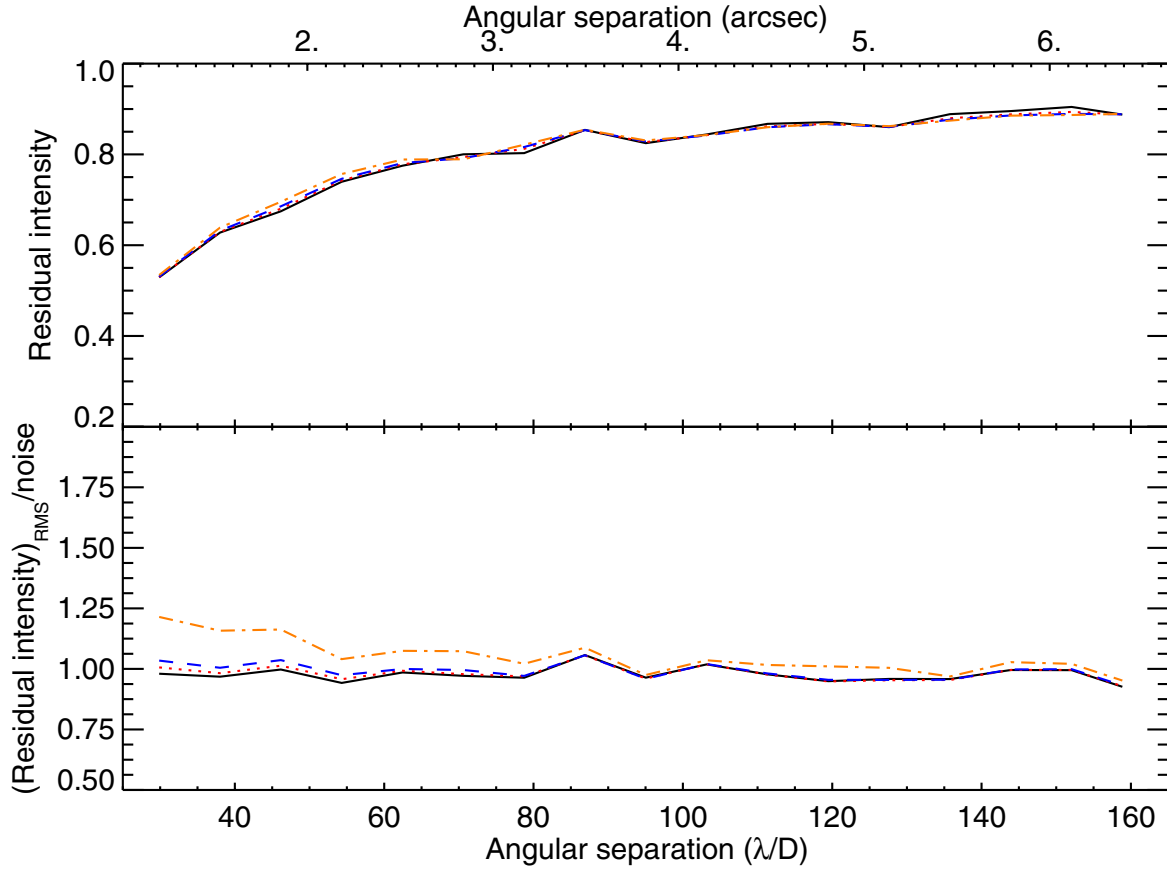
Fig. 6.— Average residual intensity of the artificial point sources normalized to their initial intensity (*top*) and ratio of the measured dispersion of the residual source intensities over the noise in the residuals (*bottom*). The solid (black), dotted (red), dashed (blue) and dot-dashed (orange) lines are respectively for point source intensities yielding S/N of 3, 6, 10 and 25 in the final residual image.
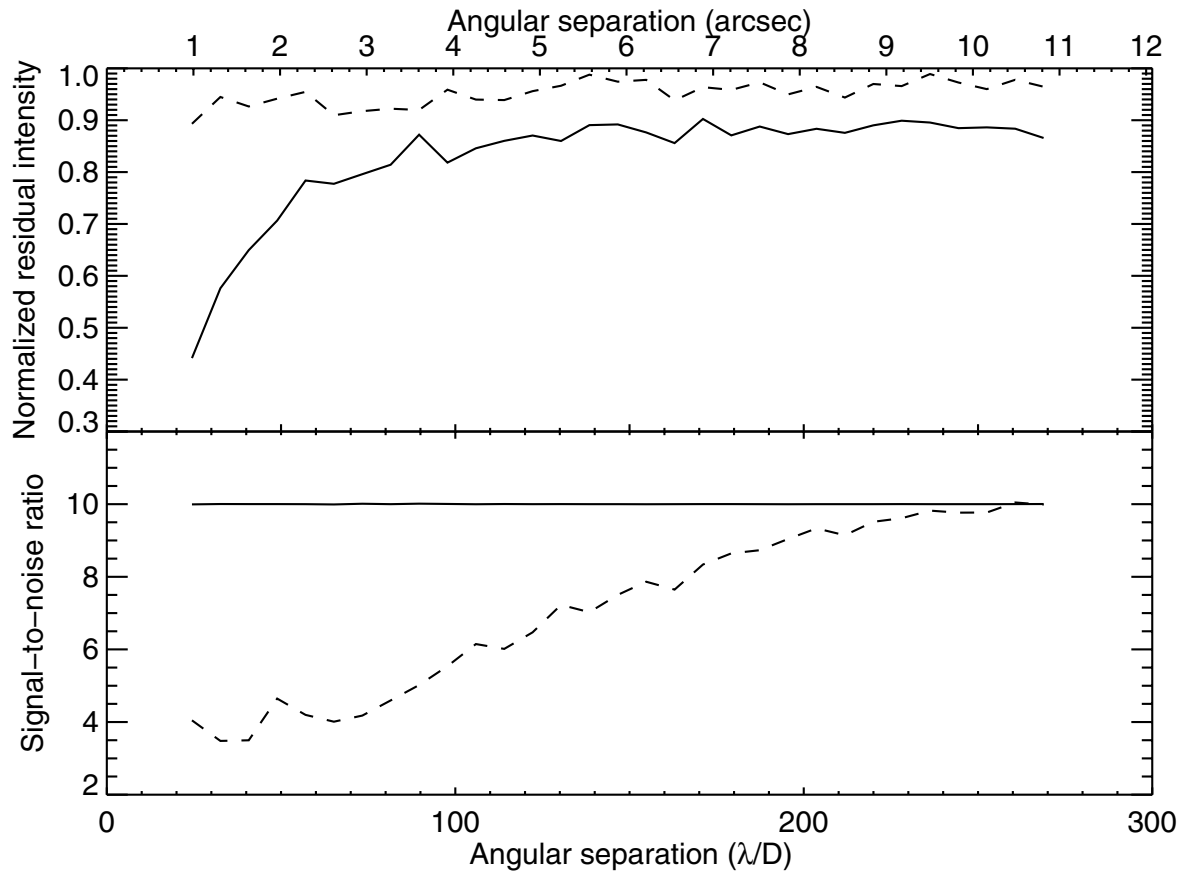
Fig. 7.— Same as Fig. 2. The solid and dashed lines are respectively for the algorithm presented in this paper and the algorithm of Marois et al. (2006).
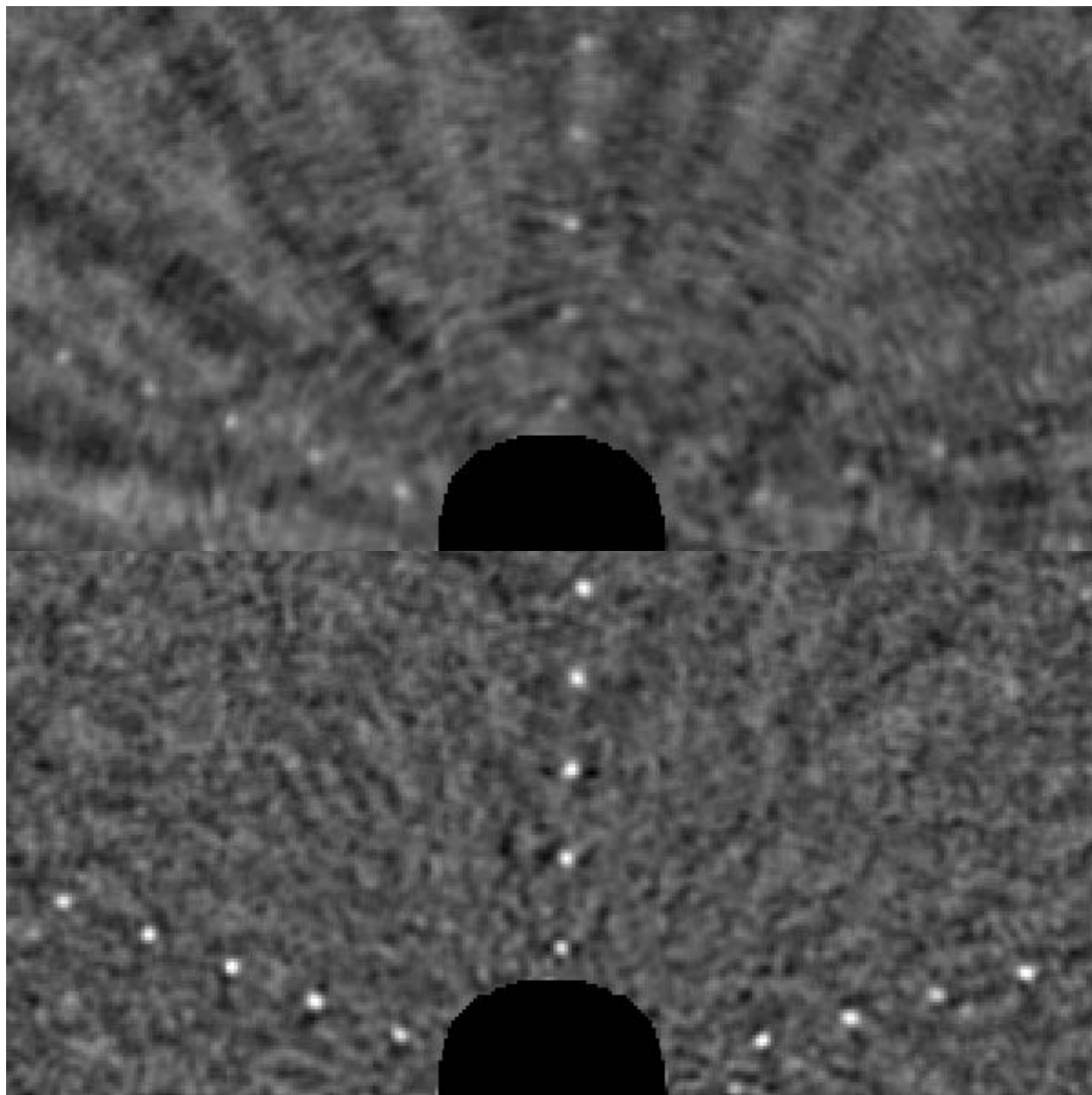
Fig. 8.— Residual S/N image (including artificial point sources) using the algorithm of Marois et al. (2006) (*top*) and the new algorithm (*bottom*). Both panels are shown with a (-5,+10) intensity range. Each panel is $6\rlap{.}''5$ by $3\rlap{.}''25$. The images have been convolved by a circular aperture of diameter equal to W. The saturated region at the center of the PSF is masked out.
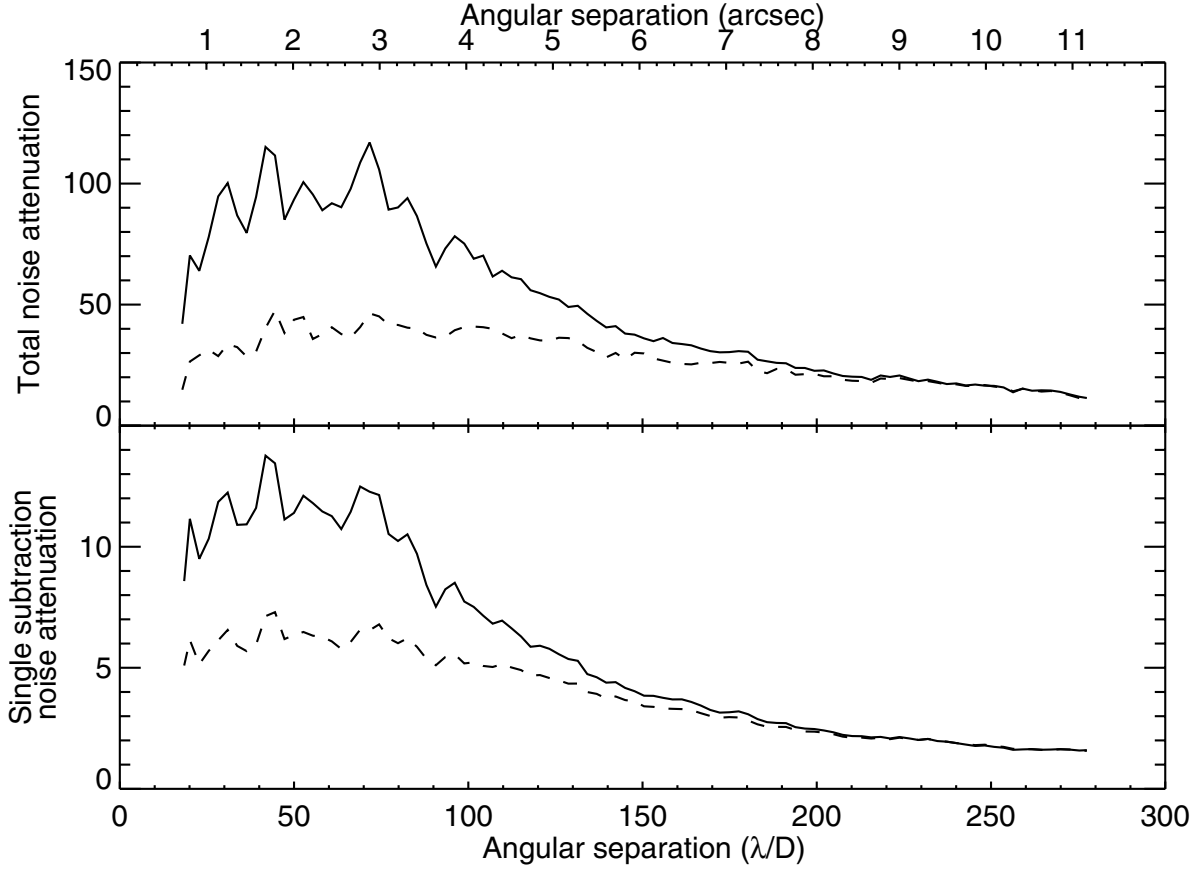
Fig. 9.— Noise attenuation resulting from a single reference image subtraction (*bottom*) and total noise attenuation (*top*). The dashed and solid lines are respectively for the algorithm of Marois et al. (2006) and the new algorithm. The attenuations have been corrected for the partial subtraction of point sources. Before computation of the initial noise level, a 7×7 PSF FWHM median filter was subtracted from the images to remove the low spatial frequency structures that do not prevent point source detection.
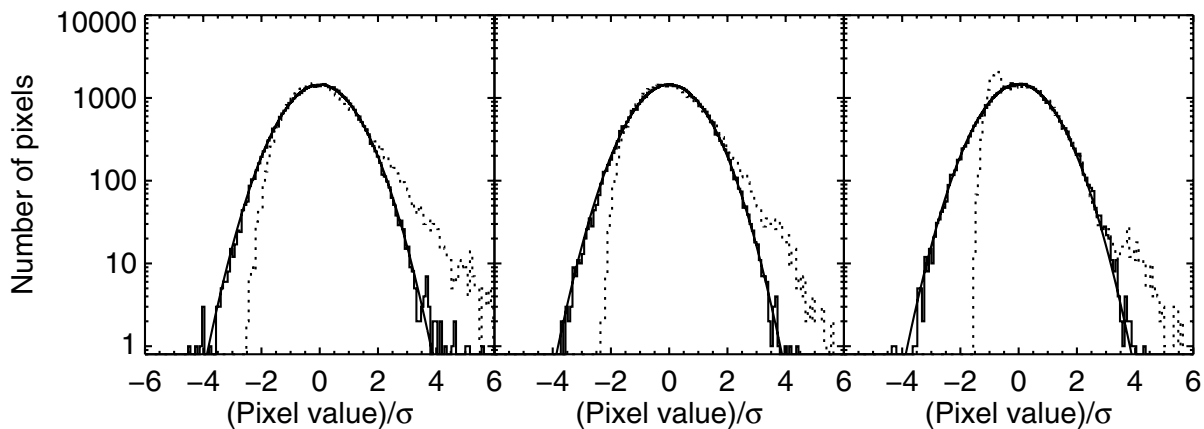
Fig. 10.— Statistical distributions of the pixel values of one original S/N image after subtraction of a radial profile (*dotted line*) and of the final S/N residual image (*solid line*) obtained with the new algorithm. From left to right, the three panels are for angular separations of 25, 50 and 150 λ/D respectively. Both images have been convolved by a circular aperture of diameter equal to W and annuli of area equal to 5000 $\pi(W/2)^2$ were used to obtain the distributions at each separation. The continuous solid curve shows a Gaussian distribution of unit standard deviation.
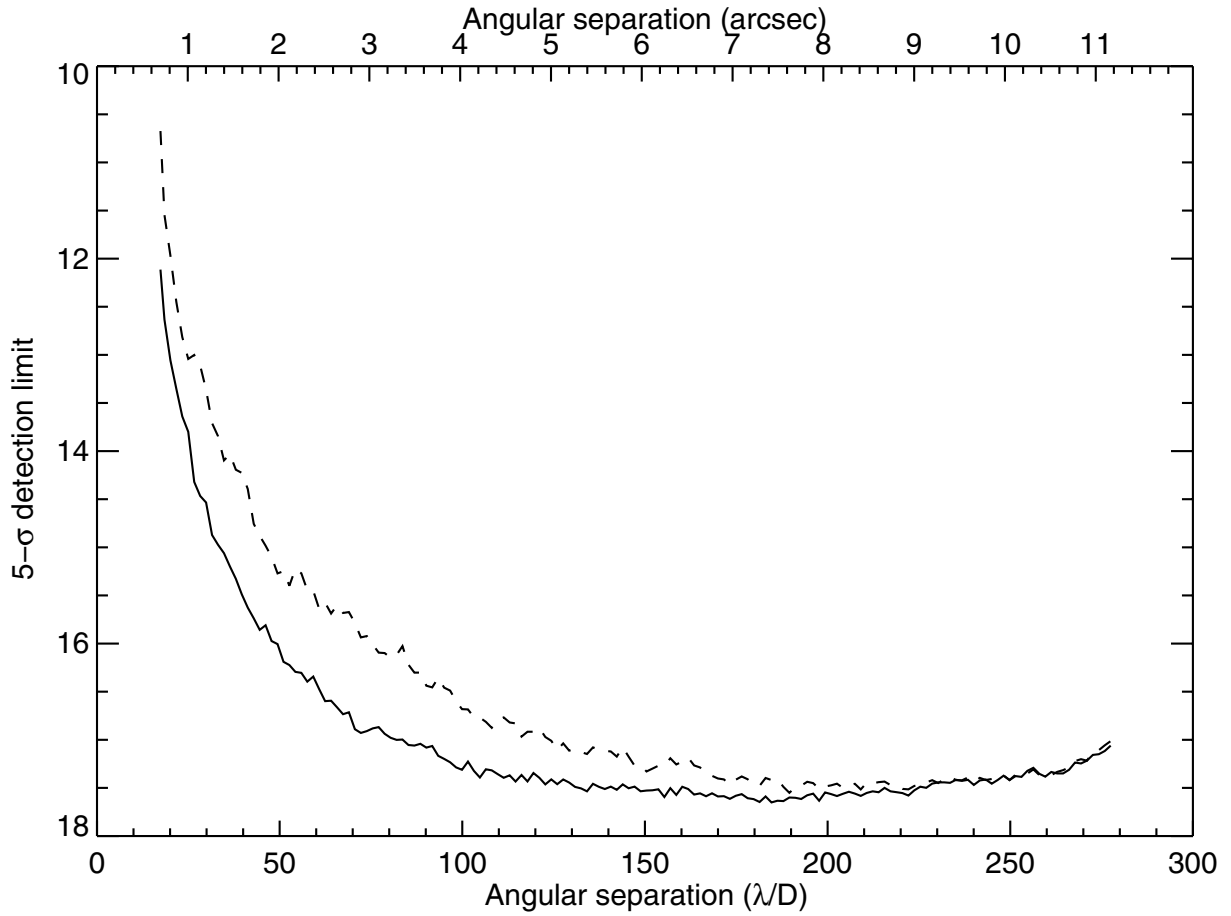
Fig. 11.— Point source detection limit. The dashed and solid lines are respectively for the algorithm of Marois et al. (2006) and the new algorithm. The detection limits have been corrected for the partial subtraction of point sources, for the anisoplanatism observed with ALTAIR and for the slight smearing of point sources during an exposure due to FOV rotation.